metals

MDPI

Article

Ultrasound-Assisted Synthesis of High-Entropy Materials for Enhanced Oxygen Evolution Electrocatalysis

Zhiyuan Wang [1,2,3], Chengxu Zhang [1], Yue Zhang [1,2] and Jue Hu [1,2,3,*]

[1] Faculty of Metallurgical and Energy Engineering, Kunming University of Science and Technology, Kunming 650093, China
[2] Key Laboratory of Unconventional Metallurgy, Kunming University of Science and Technology, Kunming 650093, China
[3] State Key Laboratory of Complex Nonferrous Metal Resources Clean Utilization, Kunming University of Science and Technology, Kunming 650093, China
* Correspondence: hujue@kust.edu.cn

Abstract: High-entropy materials (HEMs) play a significant role in the electrocatalytic oxygen evolution reaction (OER) due to their unique properties. However, there are still challenges in the preparation of HEMs for OER catalysts. In this study, the FeCoNiMnCr catalyst is synthesized for the first time using the ultrasonic hydrothermal-sintering technique and exhibits excellent performance for OER electrocatalysis. There is an optimal ultrasonic hydrothermal time and power for achieving the best OER performance. The results demonstrate that the performance of FeCoNiMnCr catalysts prepared through ultrasonic hydrothermal sintering (US-FeCoNiMnCr) is significantly improved compared with the traditional hydrothermal-sintering method. The US-FeCoNiMnCr catalyst exhibits an overpotential of 228 mV at the current density of 10 mA cm^{-2} and a Tafel slope as low as 45.39 mV dec^{-1} in an alkaline medium. Moreover, the US-FeCoNiMnCr catalyst demonstrates remarkable stability in electrocatalytic OER with a minimal potential increase observed even after 48 h. This work not only provides valuable insights into high-entropy material synthesis, but also presents a powerful electrocatalyst for water electrolysis.

Keywords: high-entropy materials; ultrasonic hydrothermal-sintering method; oxygen evolution reaction; in situ Raman

check for updates

Citation: Wang, Z.; Zhang, C.; Zhang, Y.; Hu, J. Ultrasound-Assisted Synthesis of High-Entropy Materials for Enhanced Oxygen Evolution Electrocatalysis. *Metals* **2024**, *14*, 384. https://doi.org/10.3390/met14040384

Academic Editor: Jiro Kitagawa

Received: 20 February 2024
Revised: 14 March 2024
Accepted: 19 March 2024
Published: 25 March 2024

Copyright: © 2024 by the authors. Licensee MDPI, Basel, Switzerland. This article is an open access article distributed under the terms and conditions of the Creative Commons Attribution (CC BY) license (https://creativecommons.org/licenses/by/4.0/).

1. Introduction

Since the beginning of the 21st century, the global greenhouse effect and pollution have become increasingly serious [1,2]. Finding a clean energy source to replace fossil fuels has become urgent. Hydrogen, as a non-polluting and clean energy source, has attracted widespread attention due to its high conversion efficiency, sustainability, and large-scale application [3,4]. Currently, hydrogen production is divided into two categories: hydrogen production from fossil fuels and hydrogen production from the electrolysis of water. Global hydrogen production is currently dominated by hydrogen from fossil fuels. However, hydrogen production from fossil fuels emits large amounts of carbon dioxide, which is not compatible with the current international environment. Hydrogen produced from electrolytic water is highly pure, clean, and non-polluting, but electrolytic water accounts for only 4 percent of total global hydrogen production. Nevertheless, as one of the important half-reactions in hydrogen production from electrolytic water, the oxygen evolution reaction (OER) is a four-electron transfer reaction with relative kinetics and thus requires additional electrical potential to drive the reaction [5]. In addition, an efficient electrocatalyst is required to drive the reaction kinetics for potential overshooting. Noble-metal-based electrocatalysts (gold, silver, ruthenium, platinum, iridium, etc.) also show excellent electrocatalytic performance, but their high cost limits their commercial application. Therefore, it is particularly important to find a low-cost, high-efficiency, and

promising method for the preparation of electrocatalysts. In the past, efficient OER catalysts were synthesized by transition metal institutes, such as FeNi [6], CoNi [7], FeCoNi [8], and AlFeNi [9]. Conventional binary or ternary alloys may have poor corrosion resistance due to large miscibility gaps, which hinders their further applications.

The concept of high-entropy alloys (HEAs) [10–12], also known as multi-major element alloys, was first introduced in 2004. When multiple elements are mixed in near-equal atomic ratios, the resulting alloys do not form complex intermetallic compounds but simple solid solution structures [13–16]. This emergence of HEAs challenges the traditional design concept of alloys based on mixed enthalpy and opens up a wide range of possibilities for the research and development of new materials. HEAs offer a broad alloy design space and possess unique properties, allowing for the creation of diverse multi-element active sites on catalyst surfaces [17]. High-entropy alloys have garnered widespread usage in catalysis in recent times. Zhang et al. [18] used arc and rolling techniques to synthesize $Ni_{20}Fe_{20}Mo_{10}Co_{35}Cr_{15}$, with overpotentials of 107 mV and 172 mV in acid and base solutions, respectively, when the current density is 10 $mAcm^{-2}$. Dai et al. [19] prepared MnFeCoNi with an OER overpotential of 302 mV and a current density of 10 mA cm^{-2}. Schuhamnn et al. [20] successfully synthesized a CrMnFeCoNi HEA oxygen reduction reaction (ORR) catalyst without precious metals, with almost the same performance as the commercial Pt/C. Subramanian Nellaiappan et al. [21] prepared AuAgPtPdCu for the carbon dioxide (CO_2) reduction reaction (CO_2RR) using melting and freeze-milling techniques. The Faraday efficiency of the gaseous product is about 100% at a low voltage (−0.3 V vs. hydrogen electrode (RHE)). Lei Wang et al. [22] illustrated that the prepared RuFeCoNiCu HEA electrocatalysts obtained excellent nitrogen reduction reaction (NRR) performance due to the synergistic effect of multiple active centers. HEAs have great potential in the field of catalysis due to their favorable chemical and physical properties.

Many methods have been reported for synthesizing HEAs. Hu et al. [23] used carbon thermal impingement of nanoparticles for uniform elemental mixing. In this case, thousands of temperatures are heated instantaneously. N Nader Parvin et al. [24] prepared $CoCrFeMnNiTi_{0.1}$ by the ball milling method. However, this preparation method, which employs a two-step process (i.e., solvothermal synthesis of a metal–organic framework (MOF) precursor followed by pyrolysis), is a solid-state process and is not widely enough applied. The synthesized HEA catalysts exhibited remarkable performance in oxygen evolution reactions (OERs). Given the inherent limitations of the traditional solvothermal method, which includes a cumbersome process and low yield, it is of utmost importance to devise a simplified yet highly effective process for synthesizing HEA catalysts.

For nearly two decades, ultrasound-assisted synthesis of nanomaterials has been progressing [25,26]. Ultrasound irradiation enables the liquid phase to exhibit enhanced malleability across a broad range. The cavitation effect induced by ultrasound irradiation generates significant amounts of energy. This energy enhances the mass transfer rate of reactants, subsequently accelerating the reaction rate. Locally generated high pressures and temperatures contribute to improving the selectivity of substances. Lowering the activation energy required for the reaction decreases the reaction temperature and reduces energy consumption. These advantages highlight the promising application prospects of ultrasound-assisted synthesis catalysts [27,28].

In this work, we developed an ultrasonic hydrothermal-sintering method for synthesizing high-entropy alloys. This method offers significant advantages in terms of time efficiency, reducing the hydrothermal synthesis time from 24 h to 1.5 h compared to the conventional hydrothermal-sintering method. In addition, the catalysts synthesized using this method showed superior performance in the OER compared to catalysts synthesized using the conventional hydrothermal-sintering method. The overpotential of the catalysts synthesized by the ultrasonic hydrothermal-sintering method was 19 mV lower than that of the catalysts synthesized by the conventional hydrothermal-sintering method at a current density of 10 mA cm^{-2}, which was only 228 mV. It is noteworthy that sonochemistry has been used to synthesize many MOF crystals, but the synthesis of electrocatalysts using

the ultrasonic hydrothermal method proposed in this paper has been rarely reported in previous articles. This work presents a novel synthetic route for future electrocatalyst synthesis and holds great potential for wide application.

2. Experimental Section

US-FeCoNiMnCr electrocatalysts were prepared by ultrasonic hydrothermal sintering. First, 0.25 mmol of Co $(NO_3)_2$ $6H_2O$, 0.25 mmol of Fe $(CO_2CH_3)_2$ $4H_2O$, 0.25 mmol of Ni $(NO_3)_2$ $6H_2O$, 0.25 mmol of Cr $(NO_3)_2$ $6H_2O$, 0.25 mmol of Mn $(NO_3)_2$ $4H_2O$, and 0.34 mmol of 2,5-dihydroxyterephthalic acid (H_4DOT) were dissolved in 22.5 mL of N,N-Dimethylformamide (DMF), 1.35 mL of deionized (DI) water and 1.35 mL of anhydrous ethanol (EtOH) sonicated until a homogeneous solution was formed. Then, it was transferred to the ultrasonic hydrothermal reaction apparatus, in which the ultrasonic frequency was 20 kHz, the ultrasonic power was 300 W, the continuous ultrasonic time was 10 min, the intermittent time was 30 s, and the ultrasonic time was 60 min at 120 °C (Figure 1a). Finally, the collected US-FeCoNiMnCr was washed with DI water, EtOH, and DMF and dried in a blast furnace at 70 °C overnight. After drying, the product is placed in a tube furnace. The tube furnace is pre-treated at 350 °C for 1 h and heated at 450 °C for 2 h (heating rate: 5 °C min^{-1}) after passing a mixture of H_2/Ar (5% H_2).

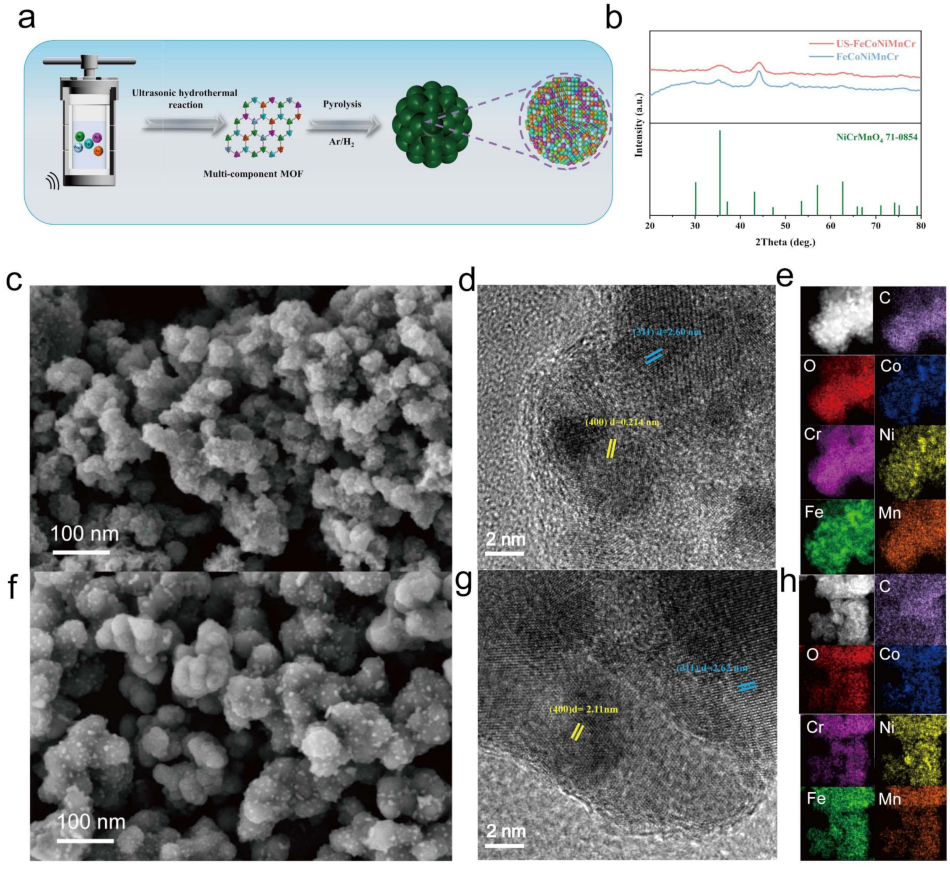

Figure 1. (**a**) The schematic diagram illustration of the synthesis process of high-entropy materials using the ultrasonic hydrothermal-sintering method. (**b**) XRD patterns of the US-FeCoNiMnCr and FeCoNiMnCr catalysts. (**c**) SEM micrograph, (**d**) TEM micrograph, and (**e**) the corresponding EDS mapping of US-FeCoNiMnCr (scale: 2.5 μm). (**f**) SEM micrograph, (**g**) TEM micrograph, and (**h**) the corresponding EDS mapping of FeCoNiMnCr (scale: 2.5 μm).

The FeCoNiMnCr electrocatalysts were fabricated using the traditional hydrothermal-sintering method. The preparation process was also hydrothermal to prepare the MOF precursor with a hydrothermal time position of 24 h. The rest of the conditions, such as the hydrothermal temperature, type of chemical reagent, filtration conditions, drying

temperature, and sintering atmosphere and temperature, were consistent with the synthesis by the ultrasonic hydrothermal-sintering method.

3. Results and Discussion

US-FeCoNiMnCr and FeCoNiMMnCr high-entropy alloy (HEA) catalysts were synthesized using ultrasonic hydrothermal-sintering and conventional hydrothermal-sintering methods. The preparation process of US-FeCoNiMnCr catalysts is shown in Figure 1a. The catalysts prepared by both methods were examined by X-ray powder diffraction (XRD). The XRD plots of both samples are consistent with the $NiCrMnO_4$ structure (CCDC: 71-0854) (Figure 1b). This shows that the addition of ultrasound does not affect the crystal structure of the catalyst. As shown in the figure, both US-FeCoNiMnCr and FeCoNiMnCr high-entropy materials show distinct characteristic peaks at 2θ = 35.5° and 43.1°, which correspond to the crystalline surfaces (311) and (400) of $NiMnO_4$, respectively. The diffraction peaks of US-FeCoNiMnCr catalysts are wider and lower than those of FeCoNiMnCr catalysts. After that, we performed the XRD characterization of the samples with different sonication times. The intensity and width of the diffraction peaks were found to be basically the same for the sonication times of 30 min and 120 min (Figure S1). This may be due to the excessive nucleation rate due to ultrasound versus the lower crystallinity due to the shorter ultrasonic hydrothermal time. In addition, based on the concept of entropy, which defines HEA as having a conformational entropy greater than 1.5 R in its random solution state, the mixing entropy of the two medium catalysts was calculated by $\Delta S_{conf} = -R\sum_{i=1}^{n} X_i ln X_i$ (where xi is the mole fraction of the i element in the random solution state) to be 1.60 R, where R is the gas constant [29,30]. This also proves that the synthesis of high-entropy alloy catalysts by ultrasonic hydrothermal sintering is feasible.

The micromorphology of the two electrocatalysts was analyzed using scanning electron microscopy (SEM) and transmission electron microscopy (TEM). Compared to the irregular shape of nanoparticles prepared by the conventional hydrothermal-sintering method, nanoparticles formed by the ultrasonic hydrothermal-sintering method have a more pronounced spherical contour, a smoother surface, and more distinct boundaries between the particles, with many smaller particles attached to their surfaces. This was attributed to the formation of cavitation bubbles in the reaction system under the action of ultrasound, which provided an interfacial region for the heterogeneous nucleation of crystal nuclei [31]. At the same time, the generation of a large number of cavitation bubbles in the liquid promotes nucleation and crystal growth, thus greatly reducing the energy required for nucleation. Consequently, this will accelerate the rate of nucleation, resulting in the production of crystal structures with smoother surfaces. In addition, the rapid formation and supersaturation of nuclei in the reaction system considerably reduce the reaction time. Energy Dispersive Spectroscopy (EDS) revealed the even distribution of the five metallic elements—iron, cobalt, nickel, manganese, and chromium. This demonstrates the successful introduction of five metal elements (Figure S2).

The high-resolution transmission electron microscopy (HRTEM) images in Figure 1d,g depict the distances between neighboring lattice stripes in different atomic structures of HEAs. The characteristic peaks at 35.5° and 43.1° of the electrocatalysts synthesized using both methods are characteristic of the face-centered cubic FCC (111) and (400) faces. This indicates the formation of single-phase FCC in US-FeCoNiMnCr and FeCoNiMnCr catalysts. Compared with the two catalysts, the crystal spacing of US-FeCoNiMnCr is d = 2.62 nm for (311) and d = 2.11 nm for (400). d = 2.60 nm for (311) and d = 2.14 nm for (400). Both crystal spacing variations are small, which is consistent with the results of the XRD test. The results of elemental mapping in Figure 1e,h show that the surfaces of US-FeCoNiMnCr and FeCoNiMnCr catalysts have a uniform distribution of Fe, Co, Ni, Mn, and Cr elements. Table S1 lists the composition and elemental ratios of the catalysts determined using ICP-OES. Five metallic elements were successfully introduced into the catalyst. Raman spectroscopy allows us to obtain detailed information about the chemical structure, crystallinity, morphology, phases, and molecular interactions of the samples. As

shown in Figure S3, the Raman spectroscopy analysis reveals two distinct broad peaks on the surfaces of the electrocatalyst particles instead of narrow peaks. The analysis of the Raman spectra shows that the D-bands' peaks of the US-FeCoNiMnCr and FeCoNiMnCr catalysts are at 1572.58 cm^{-1} and 1587.64 cm^{-1}, respectively, while the G-bands' peaks are at 1343.33 cm^{-1} and 1347.20 cm^{-1}, respectively. The peak intensity ratios are 0.854 versus 0.848, respectively. This indicates that the two electrocatalyst particles possess distinct carbon shells with varying degrees of graphitization.

X-ray photoelectron spectroscopy (XPS) was employed to investigate the modulation of electronic structure and elemental valence states in two electrocatalysts, namely US-FeCoNiMnCr and FeCoNiMnCr. Figure 2a presents the XPS spectroscopic analyses of these two electrocatalysts, confirming the successful doping of five excess metals onto the catalyst surfaces. Additionally, high-resolution C 1s XPS spectra (Figure S4a) verified the presence of carbon nanotubes with C=C/C (284.8 eV) bonds.

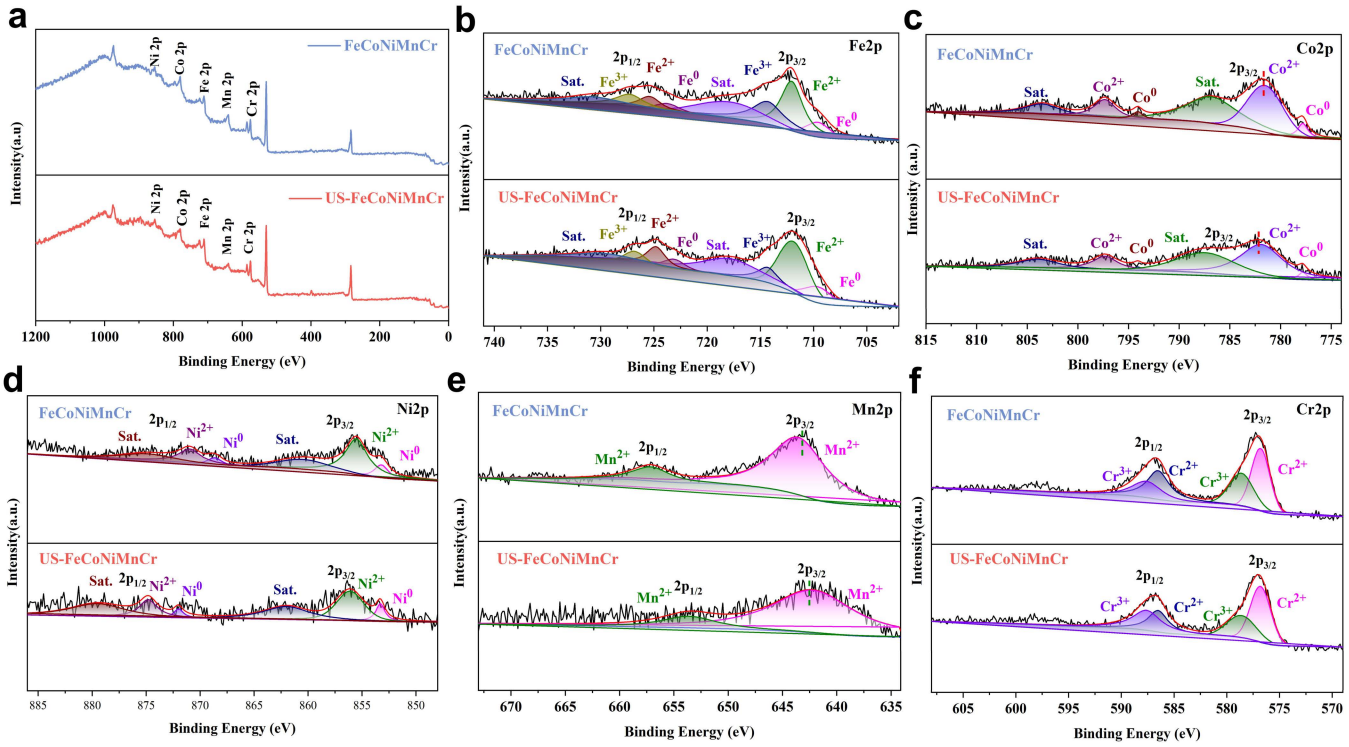

Figure 2. (**a**) XPS survey spectra, (**b**) Fe 2p, (**c**) Co 2p, (**d**) Ni 2p, (**e**) Mn 2p, and (**f**) Cr 2p of US-FeCoNiMnCr and FeCoNiMnCr catalysts.

Figure 2b–f illustrate the mixed metallic state of the metallic elements in the US-FeCoNiMnCr and FeCoNiMnCr electrocatalysts. Both electrocatalysts exhibit a prominent peak at the Fe $2p_{3/2}$ core energy level. In the high-resolution Fe 2p spectra (Figure 2b), distinct peaks are observed at the Fe $2p_{3/2}$ core energy level for both US-FeCoNiMnCr and FeCoNiMnCr electrocatalysts. The binding energies for US-FeCoNiMnCr are located at 709.75 eV, 712.11 eV, 714.50 eV, and 718.37 eV, while for FeCoNiMnCr, they are at 709.52 eV, 711.85 eV, 714.15 eV, and 718.02 eV. These binding energies correspond to the metals Fe, Fe^{2+}, Fe^{3+}, and their respective satellite peaks. The Co $2p_{3/2}$ energy levels in Figure 2c exhibit two peaks representing the metal Co (777.87 eV) and the Co^{2+} phase (781.77 eV) for the US-FeCoNiMnCr electrocatalyst, and two peaks for the metal Co (777.90 eV) and the Co^{2+} phase (781.12 eV) for the FeCoNiMnCr electrocatalyst, indicating different oxidation states of cobalt. The Ni 2p XPS spectrum (Figure 2d) displays three spin-orbit peaks corresponding to the metal Ni (853.50 eV), Ni^{2+} (856.12 eV), and a satellite peak (862.25 eV) [32]. The significant presence of high-valent nickel suggests that the catalyst exhibits good OER activity, aligning with our expectations.

As depicted in Figure 2e, the energy level of Mn $2p_{3/2}$ indicates Mn^{2+} (641.90 eV) for the sonicated sample, whereas the conventional sample exhibits Mn^{2+} (641.40 eV). Figure 2f illustrates the energy level diagrams for the metal Cr, displaying Cr^{2+} (576.87 eV) and Cr^{3+} (578.75 eV) in the US-FeCoNiMnCr sample, and Cr^{2+} (576.75 eV) and Cr^{3+} (578.65 eV) in the FeCoNiMnCr sample. Notably, the binding energies of both Mn and Co metals experienced more significant shifts. In comparison to the FeCoNiMnCr electrocatalyst, the peaks corresponding to the Mn $2p_{3/2}$ species in the US-FeCoNiMnCr electrocatalyst shifted negatively, resulting in reduced binding energy [33]. Conversely, the peaks associated with the Co $2p_{3/2}$ species shifted positively, leading to increased binding energy. These findings suggest that the electronic structures of Co and Mn metal atoms change the US-FeCoNiMnCr electrocatalysts, facilitating enhanced electron transfer from Co to Mn atoms [34]. In addition, these species with high valence states can enhance OER kinetics to provide highly intrinsic activity [35,36]. In the O 1s region (Figure S4b), O in the HEA catalysts coexists as metal–oxygen (M−O), surface-adsorbed oxygen or hydroxyl groups, and surface-physiosorbed or chemisorbed molecular water [37].

The electrocatalytic activity of the catalyst composite electrodes was evaluated using a three-electrode setup in an O_2-saturated 1M KOH electrolyte to assess the OER activity. The reference electrode used was Hg/HgO. The catalyst's overpotential was typically observed at a current density of 10 mA cm^{-2}, which served as a measure of its performance. The linear swept voltammetry curves depicted in Figure 3a demonstrate that the US-FeCoNiMnCr electrocatalysts exhibit an exceptionally low overpotential of 228 mV at a current density of 10 mA cm^{-2}, surpassing that of the FeCoNiMnCr electrocatalysts (247 mV). Additionally, the Tafel slope of the US-FeCoNiMnCr catalyst is 45.39 mV dec^{-1}, which is lower than that of the scandium iron cobalt nickel manganese catalyst (48.80 mV dec^{-1}) (Figure 3b). This observation suggests that the US-FeCoNiMnCr electrocatalyst possesses faster surface OER kinetics. The electrochemically active surface area (ECSA) of the electrocatalysts is directly proportional to the electrochemical double layer capacitance (C_{dl}), which can be determined through cyclic voltammetry (CV) measurements correlated with the scan rate (Figure S5), as illustrated in Figure 3c. Notably, the C_{dl} value for the US-FeCoNiMnCr electrocatalysts is 5.90 mF cm^{-2}, exceeding that of the FeCoNiMnCr electrocatalysts with 4.70 mF cm^{-2}. To further explain the electrode reaction kinetics during the OER process, electrochemical impedance spectroscopy (EIS) tests were taken. The Nyquist plots in Figure 3d show that the charge transfer resistance (R_{ct}) of the US-FeCoNiMnCr electrocatalyst is the lowest at approximately 1.25 Ω, which is significantly smaller than that of the FeCoNiMnCr electrocatalyst (4.31 Ω) at an overpotential of 300 mV in 1 M KOH. The high current density limit (C_{dl}) of the US-FeCoNiMnCr catalyst indicates its high ECSA. In Figure S6, the US-FeCoNiMnCr catalysts underwent OER-specific activity ECSA normalization, which highlights the exceptional intrinsic activity of the catalysts. These results indicate that the US-FeCoNiMnCr surface exhibits higher electronic conductivity and a faster charge transfer rate during the electrochemical OER process. The OER activities of the US-FeCoNiMnCr and FeCoNiMnCr electrocatalysts are characterized by low overpotentials and small Tafel slopes, which exceed the OER activities under the same conditions as many recently reported high-entropy electrocatalysts (Figure 3e) [19,38–47].

We also carried out electrochemical characterization at different ultrasonic powers and ultrasonic times and found that the best electrochemical characteristics were obtained at an ultrasonic frequency of 20 kHz, a power of 300 W, and a time of 60 min (Figure S7) [48].

Figure 4a,b were used to investigate the dependence of the catalysts on the pH value. Both the US-FeCoNiMnCr and FeCoNiMnCr catalysts showed increased activity at pH = 13–14. To precisely elucidate the relationship between oxygen evolution reaction (OER) reactivity and pH, we used the proton reactivity level on the RHE scale (ρRHE, ρRHE = log(*j*)/pH). It is a criterion for determining the dependence of OER reaction kinetics on proton activity [49,50]. When the ρRHE value approaches 1, it indicates enhanced pH dependence of the catalyst. As shown in Figure 4c and Figure S8, the ρRHE value of US-FeCoNiMnCr is comparable to that of FeCoNiMnCr, and the ρRHE value is much less than 1. This implies that the

two electrocatalysts exhibit the same OER mechanism [51,52]. Impressively, the turnover frequency (TOF) of the US-FeCoNiMnCr electrocatalyst is much higher than that of the FeCoNiMnCr electrocatalyst in alkaline media, as shown in Figure 4d. This indicates that the US-FeCoNiMnCr electrocatalyst produces a greater number of oxygen molecules than the FeCoNiMnCr electrocatalyst under the same potential conditions.

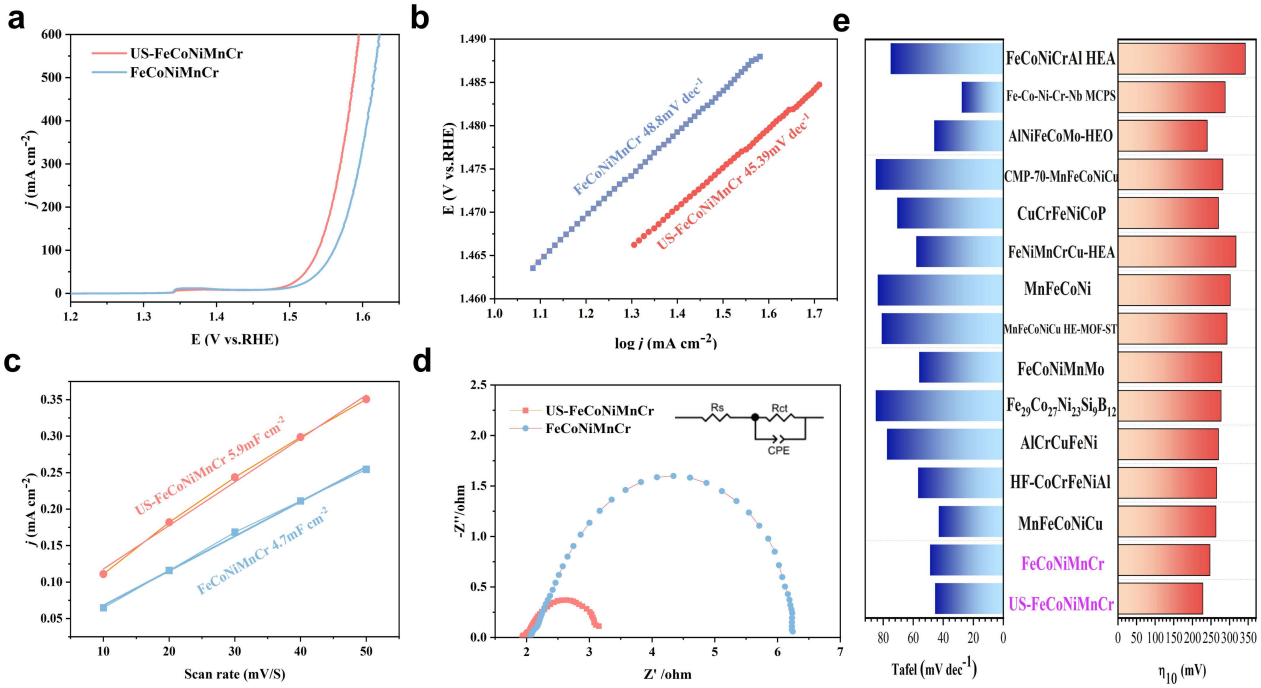

Figure 3. Electrocatalytic performance of US-FeCoNiMnCr and FeCoNiMnCr catalysts in 1.0 M KOH solution at room temperature. (**a**) IR-corrected polarization curves, (**b**) Tafel plots, (**c**) linear relationship between catalyst C_{dl} and scan rate, (**d**) Nyquist plots, (**e**) comparison with other recently reported overpotentials at 10 mA cm^{-2} and Tafel slopes of high-entropy materials.

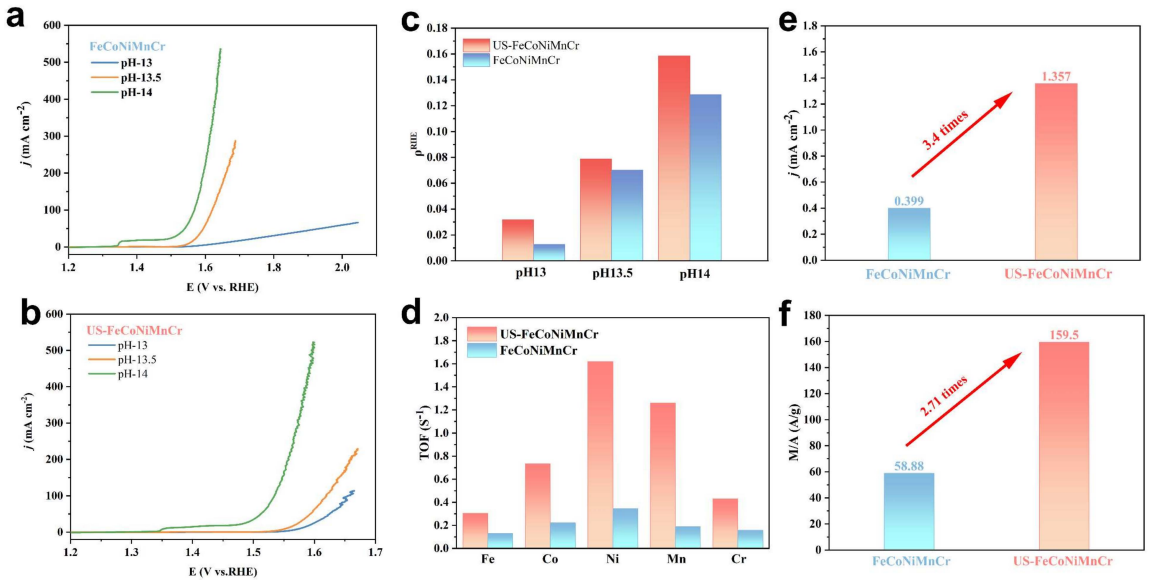

Figure 4. Polarization curves of (**a**) FeCoNiMNCr and (**b**) US-FeCoNiMNCr in different environments. (**c**) Comparison of ρRHE. (**d**) TOF of US-FeCoNiMnCr and FeCoNiMnCr catalysts at an overpotential of 300 mV. (**e**) Comparison of area-specific activity at an overpotential of 300 mV. (**f**) Comparison of mass activity.

Afterwards, we performed a pore size analysis on both electrocatalysts (Figure S9), and we found that US-FeCoNiMnCr has more small pores relative to FeCoNiMnCr. Therefore, the porosity of US-FeCoNiMnCr may provide more catalytically active sites and increase charge and mass transport. In Figure 4f, the mass activity (MA) value of US-FeCoNiMnCr is capable of up to 159.50 A g^{-1}, which is much higher than the MA value of FeCoNiMnCr (with a value of 58.88 A g^{-1}). Figure 4e reveals that the current density per unit mass for the catalyst for US-FeCoNiMnCr (1.357 mA cm^{-2}) is higher than the value observed in FeCoNiMnCr (0.399 mA cm^{-2}). From the above analytical results, it can be seen that US-FeCoNiMnCr exhibits excellent catalytic OER performance in terms of lower Tafel slopes and overpotentials.

In addition, we performed in situ Raman analyses of both catalysts. As shown in Figure 5a,b, when the applied voltage is lower than 1.0 V, US-FeCoNiMnCr has a weak peak around 605 cm^{-1}, which is attributed to the vibrational mode of M–O. When the voltage is increased from 1.0 V to 1.4 V (relative to Hg/HgO), the initial Raman peak of US-FeCoNiMnCr at 605 cm^{-1} disappears, followed by a pair of new peaks at 453 cm^{-1} ($\delta(Ni^{III}–O)$) and a pair of new peaks at 556 cm^{-1} ($\nu(Ni^{III}–O)$), attributed to the e_g bonding vibration and the A_{1g} stretching vibrational bonding of NiOOH; this reveals that the catalyst undergoes structural remodeling during the OER process. As shown in Figure 5b, the redox potential of the FeCoNiMnCr catalyst is higher than that of US-FeCoNiMnCr. This also implies that the US-FeCoNiMnCr catalyst is more prone to electrochemical oxidation in terms of energy to increase OER [53,54].

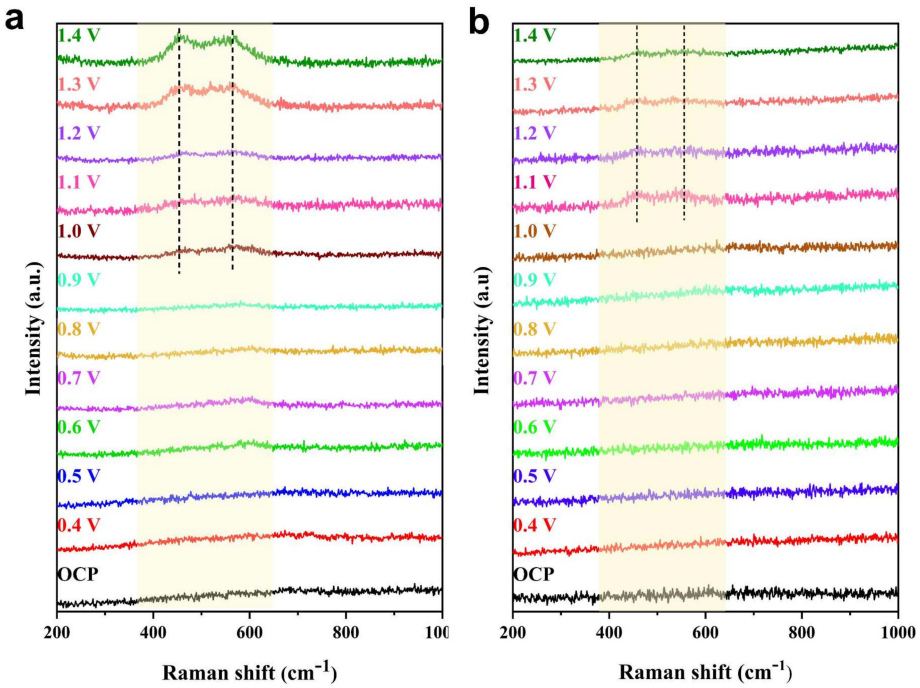

Figure 5. In situ Raman spectra of (**a**) US-FeCoNiMnCr and (**b**) FeCoNiMnCr at different potentials.

Durability is a crucial element in assessing the merits of a catalyst, particularly under high current density conditions, to ensure its long-term stability in practical electrocatalytic applications. To investigate the stability of the catalysts, chrono-potential tests were conducted. The stability tests were performed on two polymetallic high-entropy catalysts for 48 h at a current density of 100 mA cm^{-2}. As shown in Figure 6, the HEA polymetallic high-entropy catalysts prepared by the ultrasonic hydrothermal-sintering method have remarkable long-term stability. After the stability test, the potential of US-FeCoNiMnCr at 100 mA cm^{-2} remained almost unchanged. We conducted the Raman characterization of the samples after 48 h of stability and observed that the positions of the M-O bonds in the US-FeCoNiMnCr electrocatalysts did not exhibit significant shifts.

This also indicates the excellent durability of our catalysts prepared by the ultrasonic hydrothermal-sintering method.

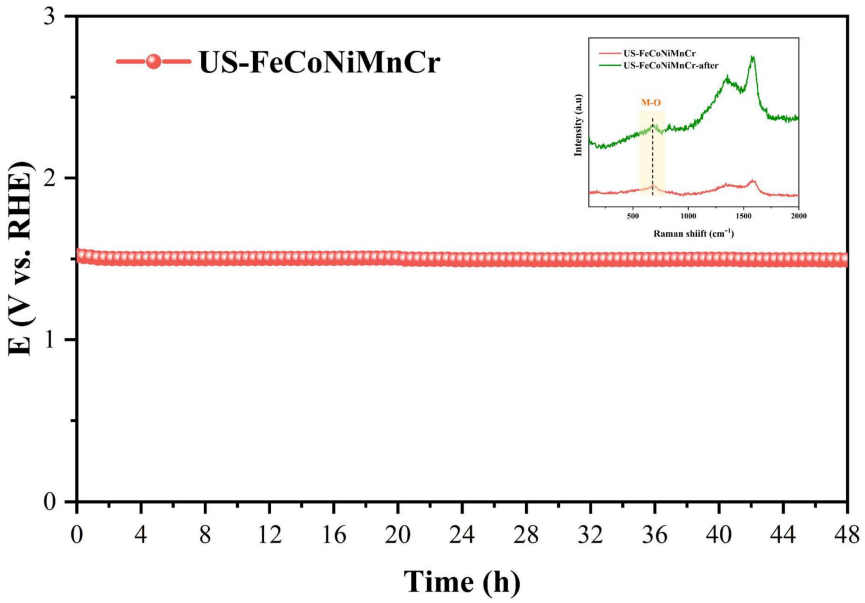

Figure 6. Chronopotentiometry measurement of US-FeCoNiMnCr catalyst at a current density of 100 mA cm^{-2} in a 1.0 M KOH solution at room temperature. Inset: Raman spectra of US-FeCoNiMnCr before and after stability test.

4. Conclusions

In this study, we compared the catalytic properties synthesized by the ultrasonic hydrothermal sintering with conventional hydrothermal sintering. Both methods successfully synthesized high-entropy alloy materials. However, the ultrasonic hydrothermal synthesis method has significant advantages over the conventional method, including lower time costs and higher energy efficiency. The catalysts obtained by ultrasonic hydrothermal sintering have lower overpotentials and smaller Tafel slopes than those obtained by conventional hydrothermal sintering. In addition, it exhibited a good durability of 48 h. It was shown by in situ Raman spectra that the US-FeCoNiMnCr catalyst is more prone to electrochemical oxidation in terms of energy to increase OER. This study presents a rational method for the preparation of HEA electrocatalysts with MOF precursors using ultrasound-assisted hydrothermal synthesis. This work provides a new method for synthesizing other electrocatalysts.

Supplementary Materials: The following supporting information can be downloaded at: https://www.mdpi.com/article/10.3390/met14040384/s1, Figure S1: The EDS image of (a) FeCoNiMnCr and (b) US-FeCoNiMnCr; Figure S2: Raman spectra of FeCoNiMnCr and US-FeCoNiMnCr; Figure S3: XPS (a) C 1s and (b) O 1s spectra of FeCoNiMnCr and US-FeCoNiMnCr; Figure S4: Cyclic voltammogram curves of (a) US-FeCoNiMnCr and (b) FeCoNiMnCr in 1.0 M KOH; Figure S5: ECSA-normalized LSV curves of US-FeCoNiMnCr and FeCoNiMnCr catalysts; Figure S6: LSV curves of US-FeCoNiMnCr catalysts under (a) different ultrasound time, and (b) different ultrasonic powers in 1.0 M KOH; Figure S7: j plots as a function of pH on a logarithmic scale for RHE at 1.55V; Figure S8: Pore size distribution of the (a) FeCoNiMnCr and (b) US-FeCoNiMnCr catalysts; Table S1: Fe, Co, Ni, Mn, and Cr contents of the two catalysts measured by ICP-OES.

Author Contributions: Conceptualization, J.H.; Methodology, Z.W.; Software, C.Z.; Validation, Y.Z.; Formal analysis, Y.Z.; Resources, J.H.; Writing—original draft, Z.W.; Writing—review and editing, C.Z. and J.H.; Funding acquisition, J.H. All authors have read and agreed to the published version of the manuscript.

Funding: This work was supported by the National Natural Science Foundation of China (Grant No.: 52364041) and Yunnan Province (202401AV070011).

Data Availability Statement: The raw data supporting the conclusions of this article will be made available by the authors on request.

Conflicts of Interest: The authors declare no conflict of interest.

References

1. Cao, H.H.; Cao, J.D.; Wang, F.H.; Di, S.X.; Zhu, H.; Pu, M.; Bulanova, A. Composition-tunable PtCu porous nanowires as highly active and durable catalyst for oxygen reduction reaction. *Int. J. Hydrogen Energy* **2021**, *46*, 18284–18293. [CrossRef]
2. Cerchier, P.; Dabala, M.; Brunelli, K. Green synthesis of copper nanoparticles with ultrasound assistance. *Green Process. Synth.* **2017**, *6*, 311–316. [CrossRef]
3. Zhang, Y.; Zhang, C.; Mei, Y.; Le, T.; Shao, H.; Jiang, H.; Feng, Y.; Hu, J. NiFe layered double hydroxide as an efficient bifunctional catalyst for electrosynthesis of hydrogen peroxide and oxygen. *Int. J. Hydrogen Energy* **2022**, *47*, 36831–36842. [CrossRef]
4. Jiang, H.; Zhang, C.; Wang, Z.; Zhang, Y.; Le, T.; Mei, Y.; Feng, Y.; Hu, J. Enhanced two-electron oxygen reduction for hydrogen peroxide production via fine-tuning the concentration of oxygen vacancies in MoO_{3-x}. *Appl. Catal. A Gen.* **2023**, *661*, 119242. [CrossRef]
5. Qi, Q.; Tai, J.; Hu, J.; Zhang, Z.; Dai, L.; Song, H.; Shao, M.; Zhang, C.; Zhang, L. Ligand Functionalized Iron-Based Metal-Organic Frameworks for Efficient Electrocatalytic Oxygen Evolution. *ChemCatChem* **2021**, *13*, 4976–4984. [CrossRef]
6. Lim, D.; Oh, E.; Lim, C.; Shim, S.E.; Baeck, S.-H. Bimetallic NiFe alloys as highly efficient electrocatalysts for the oxygen evolution reaction. *Catal. Today* **2020**, *352*, 27–33. [CrossRef]
7. Ning, H.; Li, G.; Chen, Y.; Zhang, K.; Gong, Z.; Nie, R.; Hu, W.; Xia, Q. Porous N-Doped Carbon-Encapsulated CoNi Alloy Nanoparticles Derived from MOFs as Efficient Bifunctional Oxygen Electrocatalysts. *ACS Appl. Mater. Interfaces* **2019**, *11*, 1957–1968. [CrossRef]
8. Jiang, J.; Chang, L.; Zhao, W.; Tian, Q.; Xu, Q. An advanced FeCoNi nitro-sulfide hierarchical structure from deep eutectic solvents for enhanced oxygen evolution reaction. *Chem. Commun.* **2019**, *55*, 10174–10177. [CrossRef]
9. Liu, H.; Wang, Y.; Lu, X.; Hu, Y.; Zhu, G.; Chen, R.; Ma, L.; Zhu, H.; Tie, Z.; Liu, J.; et al. The effects of Al substitution and partial dissolution on ultrathin NiFeAl trinary layered double hydroxide nanosheets for oxygen evolution reaction in alkaline solution. *Nano Energy* **2017**, *35*, 350–357. [CrossRef]
10. Ye, Y.F.; Wang, Q.; Lu, J.; Liu, C.T.; Yang, Y. High-entropy alloy: Challenges and prospects. *Mater. Today* **2016**, *19*, 349–362. [CrossRef]
11. Jiang, L.; Langan, T.; Wood, T.; Sanders, P.; Dorin, T. Isotropy of precipitate distribution in pre-stretched Al-Cu-(Sc)-(Zr) alloys. *Scr. Mater.* **2022**, *210*, 114452. [CrossRef]
12. Sun, S.; Bai, J.; Gu, J.; Guo, K.; Morley, N.; Gao, Q.; Zhang, Y.; Esling, C.; Zhao, X.; Zuo, L. Extraordinary mechanical properties and room-temperature magnetocaloric effects in spark plasma sintered all-d-metal Ni-Co-Mn-Ti alloy. *J. Alloys Compd.* **2024**, *976*, 173406. [CrossRef]
13. Mei, Y.; Feng, Y.; Zhang, C.; Zhang, Y.; Qi, Q.; Hu, J. High-Entropy Alloy with Mo-Coordination as Efficient Electrocatalyst for Oxygen Evolution Reaction. *ACS Catal.* **2022**, *12*, 10808–10817. [CrossRef]
14. Zhang, Z.H.; Hu, J.; Li, B.; Qi, Q.L.; Zhang, Y.T.; Chen, J.; Dong, P.; Zhang, C.X.; Zhang, Y.J.; Leung, M.K.H. Recent research progress on high-entropy alloys as electrocatalytic materials. *J. Alloys Compd.* **2022**, *918*, 165585. [CrossRef]
15. Brechtl, J.; Feng, R.; Liaw, P.K.; Beausir, B.; Jaber, H.; Lebedkina, T.; Lebyodkin, M. Mesoscopic-scale complexity in macroscopically-uniform plastic flow of an $Al_{0.3}$CoCrFeNi high-entropy alloy. *Acta Mater.* **2023**, *242*, 118445. [CrossRef]
16. Xing, Y.; Li, C.J.; Mu, Y.K.; Jia, Y.D.; Song, K.K.; Tan, J.; Wang, G.; Zhang, Z.Q.; Yi, J.H.; Eckert, J. Strengthening and deformation mechanism of high-strength CrMnFeCoNi high entropy alloy prepared by powder metallurgy. *J. Mater. Sci. Technol.* **2023**, *132*, 119–131. [CrossRef]
17. Wang, Z.; You, J.; Zhao, Y.; Yao, R.; Liu, G.; Lu, J.; Zhao, S. Research progress on high entropy alloys and high entropy derivatives as OER catalysts. *J. Environ. Chem. Eng.* **2023**, *11*, 109080. [CrossRef]
18. Zhang, G.; Ming, K.; Kang, J.; Huang, Q.; Zhang, Z.; Zheng, X.; Bi, X. High entropy alloy as a highly active and stable electrocatalyst for hydrogen evolution reaction. *Electrochim. Acta* **2018**, *279*, 19–23. [CrossRef]
19. Dai, W.; Lu, T.; Pan, Y. Novel and promising electrocatalyst for oxygen evolution reaction based on MnFeCoNi high entropy alloy. *J. Power Sources* **2019**, *430*, 104–111. [CrossRef]
20. Löffler, T.; Meyer, H.; Savan, A.; Wilde, P.; Garzón Manjón, A.; Chen, Y.-T.; Ventosa, E.; Scheu, C.; Ludwig, A.; Schuhmann, W. Discovery of a Multinary Noble Metal–Free Oxygen Reduction Catalyst. *Adv. Energy Mater.* **2018**, *8*, 1802269. [CrossRef]
21. Nellaiappan, S.; Katiyar, N.K.; Kumar, R.; Parui, A.; Malviya, K.D.; Pradeep, K.G.; Singh, A.K.; Sharma, S.; Tiwary, C.S.; Biswas, K. High-Entropy Alloys as Catalysts for the CO_2 and CO Reduction Reactions: Experimental Realization. *ACS Catal.* **2020**, *10*, 3658–3663. [CrossRef]
22. Zhang, D.; Zhao, H.; Wu, X.; Deng, Y.; Wang, Z.; Han, Y.; Li, H.; Shi, Y.; Chen, X.; Li, S.; et al. Multi-Site Electrocatalysts Boost pH-Universal Nitrogen Reduction by High-Entropy Alloys. *Adv. Funct. Mater.* **2021**, *31*, 2006939. [CrossRef]
23. Yao, Y.; Huang, Z.; Xie, P.; Lacey, S.D.; Jacob, R.J.; Xie, H.; Chen, F.; Nie, A.; Pu, T.; Rehwoldt, M.; et al. Carbothermal shock synthesis of high-entropy-alloy nanoparticles. *Science* **2018**, *359*, 1489–1494. [CrossRef]

24. Akhlaghi, P.; Amirjan, M.; Parvin, N. The effect of processing parameters and heat-treatment on the microstructure and mechanical properties of PM $CoCrFeMnNiTi_{0.1}$ high-entropy alloy. *Mater. Chem. Phys.* **2021**, *257*, 123722. [CrossRef]
25. Wang, Y.; Yang, Z.; Zhang, C.; Feng, Y.; Shao, H.; Chen, J.; Hu, J.; Zhang, L. Fabricating carbon quantum dots of graphitic carbon nitride vis ultrasonic exfoliation for highly efficient H_2O_2 production. *Ultrason. Sonochemistry* **2023**, *99*, 106582. [CrossRef] [PubMed]
26. Pollet, B.G. A Short Introduction to Sonoelectrochemistry. *Electrochem. Soc. Interface* **2018**, *27*, 41. [CrossRef]
27. Hinman, J.J.; Suslick, K.S. Nanostructured Materials Synthesis Using Ultrasound. *Top. Curr. Chem.* **2017**, *375*, 12. [CrossRef] [PubMed]
28. Sancheti, S.V.; Gogate, P.R. A review of engineering aspects of intensification of chemical synthesis using ultrasound. *Ultrason. Sonochemistry* **2017**, *36*, 527–543. [CrossRef]
29. Lu, Z.P.; Wang, H.; Chen, M.W.; Baker, I.; Yeh, J.W.; Liu, C.T.; Nieh, T.G. An assessment on the future development of high-entropy alloys: Summary from a recent workshop. *Intermetallics* **2015**, *66*, 67–76. [CrossRef]
30. Miracle, D.B.; Miller, J.D.; Senkov, O.N.; Woodward, C.; Uchic, M.D.; Tiley, J. Exploration and Development of High Entropy Alloys for Structural Applications. *Entropy* **2014**, *16*, 494–525. [CrossRef]
31. Sivalingam, S.; Sen, S. Valorization of coal fly ash into nanozeolite by sonication-assisted hydrothermal method. *J. Environ. Manag.* **2019**, *235*, 145–151. [CrossRef] [PubMed]
32. Wang, D.; Liu, Z.; Du, S.; Zhang, Y.; Li, H.; Xiao, Z.; Chen, W.; Chen, R.; Wang, Y.; Zou, Y.; et al. Low-temperature synthesis of small-sized high-entropy oxides for water oxidation. *J. Mater. Chem. A* **2019**, *7*, 24211–24216. [CrossRef]
33. Chen, S.; Huang, H.; Jiang, P.; Yang, K.; Diao, J.; Gong, S.; Liu, S.; Huang, M.; Wang, H.; Chen, Q. Mn-Doped RuO2 Nanocrystals as Highly Active Electrocatalysts for Enhanced Oxygen Evolution in Acidic Media. *ACS Catal.* **2020**, *10*, 1152–1160. [CrossRef]
34. Li, F.; Li, J.; Zhou, L.; Dai, S. Enhanced OER performance of composite Co–Fe-based MOF catalysts via a one-pot ultrasonic-assisted synthetic approach. *Sustain. Energy Fuels* **2021**, *5*, 1095–1102. [CrossRef]
35. Vijay, A.; Ramanujachary, K.V.; Lofland, S.E.; Vaidya, S. Role of crystal structure and electrical polarization of an electrocatalyst in enhancing oxygen evolution performance: Bi-Fe-O system as a case study. *Electrochim. Acta* **2022**, *407*, 139887. [CrossRef]
36. Zheng, X.; Zhang, B.; De Luna, P.; Liang, Y.; Comin, R.; Voznyy, O.; Han, L.; García de Arquer, F.P.; Liu, M.; Dinh, C.T.; et al. Theory-driven design of high-valence metal sites for water oxidation confirmed using in situ soft X-ray absorption. *Nat. Chem.* **2018**, *10*, 149–154. [CrossRef] [PubMed]
37. Liu, H.; Duan, H.; Yu, J.; Qiu, C.; Yu, R.; Gao, J.; Li, S.; Du, X.; Si, Z.; Yang, S. Strong Electron Coupling Effect at the CoO/CeO_2 Interface Enables Efficient Oxygen Evolution Reaction. *ACS Mater. Lett.* **2022**, *4*, 2572–2578. [CrossRef]
38. Cui, X.; Zhang, B.; Zeng, C.; Guo, S. Electrocatalytic activity of high-entropy alloys toward oxygen evolution reaction. *MRS Commun.* **2018**, *8*, 1230–1235. [CrossRef]
39. Ding, Z.; Bian, J.; Shuang, S.; Liu, X.; Hu, Y.; Sun, C.; Yang, Y. High Entropy Intermetallic–Oxide Core–Shell Nanostructure as Superb Oxygen Evolution Reaction Catalyst. *Adv. Sustain. Syst.* **2020**, *4*, 1900105. [CrossRef]
40. Qiu, H.-J.; Fang, G.; Gao, J.; Wen, Y.; Lv, J.; Li, H.; Xie, G.; Liu, X.; Sun, S. Noble Metal-Free Nanoporous High-Entropy Alloys as Highly Efficient Electrocatalysts for Oxygen Evolution Reaction. *ACS Mater. Lett.* **2019**, *1*, 526–533. [CrossRef]
41. Yan, W.; Jiang, H.; Yi, W.; Zhao, C.; Xia, Y.; Cong, H.; Tang, L.; Cheng, G.J.; He, J.; Deng, H. High-entropy-alloy nanoparticles synthesized by laser metallurgy using a multivariate MOF. *Mater. Chem. Front.* **2022**, *6*, 2796–2802. [CrossRef]
42. Zhang, T.; Li, J.; Zhang, B.; Wang, G.; Jiang, K.; Zheng, Z.; Shen, J. High-entropy alloy CuCrFeNiCoP film of Cu-based as high-efficiency electrocatalyst for water splitting. *J. Alloys Compd.* **2023**, *969*, 172439. [CrossRef]
43. Zhao, X.; Xue, Z.; Chen, W.; Bai, X.; Shi, R.; Mu, T. Ambient fast, large-scale synthesis of entropy-stabilized metal–organic framework nanosheets for electrocatalytic oxygen evolution. *J. Mater. Chem. A* **2019**, *7*, 26238–26242. [CrossRef]
44. Li, P.; Wan, X.; Su, J.; Liu, W.; Guo, Y.; Yin, H.; Wang, D. A Single-Phase FeCoNiMnMo High-Entropy Alloy Oxygen Evolution Anode Working in Alkaline Solution for over 1000 h. *ACS Catal.* **2022**, *12*, 11667–11674. [CrossRef]
45. Wang, H.; Wei, R.; Li, X.; Ma, X.; Hao, X.; Guan, G. Nanostructured amorphous $Fe_{29}Co_{27}Ni_{23}Si_9B_{12}$ high-entropy-alloy: An efficient electrocatalyst for oxygen evolution reaction. *J. Mater. Sci. Technol.* **2021**, *68*, 191–198. [CrossRef]
46. Liu, L.-H.; Li, N.; Han, M.; Han, J.-R.; Liang, H.-Y. Scalable synthesis of nanoporous high entropy alloys for electrocatalytic oxygen evolution. *Rare Met.* **2022**, *41*, 125–131. [CrossRef]
47. Ma, P.; Zhang, S.; Zhang, M.; Gu, J.; Zhang, L.; Sun, Y.; Ji, W.; Fu, Z. Hydroxylated high-entropy alloy as highly efficient catalyst for electrochemical oxygen evolution reaction. *Sci. China Mater.* **2020**, *63*, 2613–2619. [CrossRef]
48. Kim, J.-H.; Son, B.-R.; Yoon, D.-H.; Hwang, K.-T.; Noh, H.-G.; Cho, W.-S.; Kim, U.-S. Characterization of blue $CoAl_2O_4$ nano-pigment synthesized by ultrasonic hydrothermal method. *Ceram. Int.* **2012**, *38*, 5707–5712. [CrossRef]
49. Huang, Z.-F.; Xi, S.; Song, J.; Dou, S.; Li, X.; Du, Y.; Diao, C.; Xu, Z.J.; Wang, X. Tuning of lattice oxygen reactivity and scaling relation to construct better oxygen evolution electrocatalyst. *Nat. Commun.* **2021**, *12*, 3992. [CrossRef]
50. Chen, X.; Wang, Q.; Cheng, Y.; Xing, H.; Li, J.; Zhu, X.; Ma, L.; Li, Y.; Liu, D. S-Doping Triggers Redox Reactivities of Both Iron and Lattice Oxygen in FeOOH for Low-Cost and High-Performance Water Oxidation. *Adv. Funct. Mater.* **2022**, *32*, 2112674. [CrossRef]
51. Wang, F.; Zou, P.; Zhang, Y.; Pan, W.; Li, Y.; Liang, L.; Chen, C.; Liu, H.; Zheng, S. Activating lattice oxygen in high-entropy LDH for robust and durable water oxidation. *Nat. Commun.* **2023**, *14*, 6019. [CrossRef] [PubMed]
52. Tomar, A.K.; Pan, U.N.; Kim, N.H.; Lee, J.H. Enabling Lattice Oxygen Participation in a Triple Perovskite Oxide Electrocatalyst for the Oxygen Evolution Reaction. *ACS Energy Lett.* **2023**, *8*, 565–573. [CrossRef]

53. Hu, J.; Guo, T.; Zhong, X.; Li, J.; Mei, Y.; Zhang, C.; Feng, Y.; Sun, M.; Meng, L.; Wang, Z.; et al. In Situ Reconstruction of High-Entropy Heterostructure Catalysts for Stable Oxygen Evolution Electrocatalysis under Industrial Conditions. *Adv. Mater.* **2024**, 2310918. [CrossRef]
54. Ting, N.-H.; Nguyen, T.X.; Lee, C.-H.; Chen, Y.-C.; Yeh, C.-H.; Chen, H.-Y.T.; Ting, J.-M. Composition-controlled high entropy metal glycerate as high-performance electrocatalyst for oxygen evolution reaction. *Appl. Mater. Today* **2022**, *27*, 101398. [CrossRef]

Disclaimer/Publisher's Note: The statements, opinions and data contained in all publications are solely those of the individual author(s) and contributor(s) and not of MDPI and/or the editor(s). MDPI and/or the editor(s) disclaim responsibility for any injury to people or property resulting from any ideas, methods, instructions or products referred to in the content.